

The predictability of large-scale wind-driven flows

A. Mahadevan^{1,*}, J. Lu², S. P. Meacham³, and P. Malanotte-Rizzoli²

¹Ocean Process Analysis Laboratory, University of New Hampshire, Durham, NH 03824, USA

*presently at: Dept. of Applied Mathematics and Theoretical Physics University of Cambridge, Silver Street, Cambridge, CB3 9EW, UK

²Dept. of Earth, Atmospheric and Planetary Sciences, MIT, 77 Massachusetts Avenue, Cambridge, MA 02139, USA

³Atmospheric and Environmental Research, 131 Hartwell Avenue, Lexington, MA 02421, USA

Received: 18 September 2000 – Revised: 23 April 2001 – Accepted: 2 July 2001

Abstract. The singular values associated with optimally growing perturbations to stationary and time-dependent solutions for the general circulation in an ocean basin provide a measure of the rate at which solutions with nearby initial conditions begin to diverge, and hence, a measure of the predictability of the flow. In this paper, the singular vectors and singular values of stationary and evolving examples of wind-driven, double-gyre circulations in different flow regimes are explored. By changing the Reynolds number in simple quasi-geostrophic models of the wind-driven circulation, steady, weakly aperiodic and chaotic states may be examined. The singular vectors of the steady state reveal some of the physical mechanisms responsible for optimally growing perturbations. In time-dependent cases, the dominant singular values show significant variability in time, indicating strong variations in the predictability of the flow. When the underlying flow is weakly aperiodic, the dominant singular values covary with integral measures of the large-scale flow, such as the basin-integrated upper ocean kinetic energy and the transport in the western boundary current extension. Furthermore, in a reduced gravity quasi-geostrophic model of a weakly aperiodic, double-gyre flow, the behaviour of the dominant singular values may be used to predict a change in the large-scale flow, a feature not shared by an analogous two-layer model. When the circulation is in a strongly aperiodic state, the dominant singular values no longer vary coherently with integral measures of the flow. Instead, they fluctuate in a very aperiodic fashion on mesoscale time scales. The dominant singular vectors then depend strongly on the arrangement of mesoscale features in the flow and the evolved forms of the associated singular vectors have relatively short spatial scales. These results have several implications. In weakly aperiodic, periodic, and stationary regimes, the mesoscale energy content is usually relatively low and the predictability of the wind-driven circulation is determined by the large-scale structure of the flow. In the more realistic, strongly

chaotic regime, in which energetic mesoscale eddies are produced by the meandering of the separated western boundary current extension, the predictability of the flow locally tends to be a stronger function of the local mesoscale eddy structure than of the larger scale structure of the circulation. This has a broader implication for the effectiveness of different approaches to forecasting the ocean with models which sequentially assimilate new observations.

1 Introduction

The prediction of ocean currents and ocean circulation on different spatial and temporal scales has emerged as an important scientific pursuit over the last decade. Particular attention has been devoted to the prediction of mesoscale processes that characterize energetic frontal systems, such as the Western Boundary Current (WBC) systems, and their extensions, of which the Gulf Stream in the North Atlantic and the Kuroshio in the North Pacific are prominent examples. For such nonlinear systems, however, prediction is ultimately limited by the predictability of the system itself, which depends on its dynamic instabilities. Hence, there is the need to investigate and to understand the intrinsic predictability of the types of flow considered in this study. Strong oceanic frontal systems are characterized by the intermittent appearance of energetic events, such as meandering and ring formation. The classical studies of barotropic, baroclinic and mixed quasi-geostrophic instabilities (Pedlosky, 1987) have shed much light on the fundamental mechanisms responsible for the growth of mesoscale meandering events. In particular, the classical linear eigenvalue analysis of the normal modes of the system reveals the energy pathways that can support meander growth. Such analytical or semi-analytical approaches are, however, limited to simplified flows, of which a unidirectional, steady and along-stream invariant jet is the canonical example. (See, for instance, the linear theories of infinitely long, straight WBCs of Ierley and Young (1991) and Berloff and Meacham (1998), among others.) Linear in-

stability theory can be extended by considering basic flows that are slowly varying in time and/or space, but such treatments generally require that the time scale or the along-stream length scale of the basic state be long in comparison to the intrinsic time and length scales of the instabilities. Exceptions to this constraint are studies based on Floquet analysis (Lorenz, 1972) which, however, require that the basic state be periodic in time or space.

In a real system, such as the Gulf Stream and its extension, the ocean jet is convoluted and time-dependent, and exhibits strong along-stream variations. The fact that the spatial and temporal inhomogeneities of such current systems occur on scales comparable to those suggested by the above instability theories is a testimony to the power of these theories in exposing the underlying physical mechanisms responsible for synoptic scale variability. However, the spatial-temporal inhomogeneity of the ocean also means that the classical instability theories are limited in their predictive ability. Indeed, it is difficult to even choose an appropriate reference or basic state in which to apply a linear stability theory. A realistic oceanic frontal flow, such as the Gulf Stream system, is more appropriately thought of as a chaotic nonlinear system. As such, it possesses the defining characteristic of chaotic systems, with a sensitive dependence on initial conditions. Thus, the following broad question exists: ‘‘How predictable is a given time-dependent flow?’’ This needs to be addressed by constructing well defined measures of predictability. One such quantifiable measure is the rate of divergence of two oceanic flows differing slightly from each other at initial time, i.e. the rate of divergence of neighboring solution trajectories. A second useful measure is the evaluation of the spatial structure and localization of the fastest growing perturbations over a prescribed time interval. Since the ocean is an evolving, fully nonlinear system, a complete answer to the question of ‘‘How predictable is the oceanic circulation?’’ would require a detailed study of the phase space of the flow for some distance from a specified segment of the model trajectory. With existing techniques, this is too difficult a task except for very constrained flows. However, by forsaking a description of the nonlinear evolution of perturbations for a linear approximation, it is possible to tackle the complex spatial and temporal inhomogeneities in a nonlinearly evolving basic state. Two mutually related techniques that can be used for such studies have been developed and extensively used in meteorology. They are the singular vector analysis, first introduced by Lorenz (1965), and the generalized stability analysis, proposed by Farrell and Ioannou (1996a,b). These methods have been recently used in the oceanographic context by Farrell and Moore (1992, 1993); Moore and Mariano (1999); Moore (1999) among others. In the Moore and Mariano (1999) study, the generalized stability analysis is applied to a QG numerical model of the Gulf Stream, defined by the open boundary conditions of Charney (1955) as a jet entering an open ocean domain where it undergoes intense meandering associated with its intrinsic instabilities. The analysis is carried out for a localized sector of the frontal jet, leading to the fastest growing perturbations, the so-called optimal per-

turbations related to meander growth of the front itself and to localized eddy formation and interactions with the main jet. Such an open ocean model, however, cannot address the basic features of the subtropical gyre circulation that crucially affect the behaviour of the Gulf Stream system. The Gulf Stream and its extension are components of the larger and intricately interlinked wind-driven circulation of the North Atlantic basin. Important properties, such as the stream separation point and its penetration scale into the interior, are determined not only by its instabilities, but also by the surface wind forcing and by the state of the large-scale circulation. Inertial recirculations south and north of the Gulf Stream profoundly affect both its instabilities and the long time variability of the whole basin, as shown by McCalpin and Haidvogel (1996) and Primeau (1999).

In this study, we address the problem of predictability of a strong oceanic frontal system, such as the Gulf Stream, but in the idealized context of a time-dependent, wind-forced, quasi-geostrophic (QG), double-gyre circulation model. Even though idealized, such a model contains important dynamical ingredients associated with embedding the Gulf Stream jet and its instabilities in the overall, nonlinear gyre circulation. We consider two types of models, a reduced gravity QG model with one active layer, and a two-layer QG model with finite total depth. In Sect. 2 of this paper, we discuss the circulation models used. In Sect. 3, we summarize the generalized stability analysis based on the evaluation of the optimal perturbations, the singular vectors, and discuss some of their interpretations. In Sect. 4, we examine the singular vectors of the steady circulations of the two models run with the same parameters and wind-forcing. We compare the flow predictability for the two systems with different instability properties. In Sect. 5, we extend the singular vector analysis to weakly aperiodic, double-gyre circulations, characterized by irregular vacillations. The singular vector analysis is further extended to strongly aperiodic flows in Sect. 6. Finally, in Sect. 7, we provide a summarizing discussion, the conclusions of the present study, and directions for future research.

2 Models

We consider two types of quasi-geostrophic ocean circulation models: a reduced gravity model with one active (upper) layer, i.e. an equivalent barotropic model, henceforth referred to as the EB model, and a two-layer model with finite total depth that is baroclinic and referred to as the 2LQG model. The governing equations describe the evolution of potential vorticity q , and are written in terms of the stream function ψ . In the 2LQG model, the upper (active) and lower layers are distinguished by subscripts 1 and 2. The equations for each layer are:

$$\partial_t q_1 + J(\psi_1, q_1) + \beta \psi_{1x} = \nu \nabla^4 \psi_1 + \frac{f w_E}{H_1} \quad (1)$$

$$\partial_t q_2 + J(\psi_2, q_2) + \beta \psi_{2x} = \nu \nabla^4 \psi_2, \quad (2)$$

where $J(A, B) \equiv \frac{\partial A}{\partial x} \frac{\partial B}{\partial y} - \frac{\partial A}{\partial y} \frac{\partial B}{\partial x}$. Here, f and β are the planetary vorticity and its gradient, ν is a uniform eddy viscosity, H_1 is the upper layer depth, and the Ekman suction velocity is

$$w_E = W w(y/L) = \hat{z} \cdot \nabla \times \frac{\boldsymbol{\tau}(y)}{\rho_0 f}, \quad (3)$$

where L is the zonal width of the basin, W is a dimensional scale for the vertical Ekman velocity, w is a dimensionless function describing the spatial pattern of the vertical Ekman velocity, \hat{z} is the unit vector normal to the Earth's surface, ρ_0 is an approximate density of seawater, and $\boldsymbol{\tau}(y)$ is the horizontal surface wind stress. The models are written using zonal and meridional Cartesian coordinates, x and y . For the EB model, Eq. (2) is absent and

$$q_1 = (\nabla^2 - L_D^{-2})\psi_1, \quad (4)$$

where the internal deformation radius, $L_D \equiv (g'H)^{1/2}/f_0$, and g' is the usual acceleration due to gravity g , multiplied by the relative density difference between the layers $\Delta\rho/\rho_0$. In the 2LQG or baroclinic model,

$$\begin{aligned} q_1 &= \nabla^2 \psi_1 + \frac{L_D^{-2}}{1+\delta} (\psi_2 - \psi_1), \\ q_2 &= \nabla^2 \psi_2 + \frac{\delta L_D^{-2}}{1+\delta} (\psi_1 - \psi_2), \end{aligned} \quad (5)$$

where $\delta = H_1/H_2$ is the ratio of upper and lower layer depths and $L_D \equiv (g'H_1 H_3/f_0^2 H)^{1/2}$. In each model, the rigid lid approximation is used and the volume of each layer is conserved.

We non-dimensionalize by scaling x and y with L , t with $(\beta L)^{-1}$, and ψ with $(fWL/\beta H_1)$, and introduce the dimensional Munk and inertial boundary layer scales,

$$\delta_M^* = \left(\frac{\nu}{\beta}\right)^{\frac{1}{3}}, \quad \delta_I^* = \left(\frac{fW}{\beta^2 H_1}\right)^{\frac{1}{2}}, \quad (6)$$

together with their dimensionless counterparts

$$\delta_M = \frac{\delta_M^*}{L}, \quad \delta_I = \frac{\delta_I^*}{L}. \quad (7)$$

The non-dimensional vorticity equations are then

$$\partial_t q_1 + \delta_I^2 J(\psi_1, q_1) + \psi_{1x} = \delta_M^3 \nabla^4 \psi_1 + w(y) \quad (8)$$

$$\partial_t q_2 + \delta_I^2 J(\psi_2, q_2) + \psi_{2x} = \delta_M^3 \nabla^4 \psi_2. \quad (9)$$

Introducing $\lambda = L/L_D$, the dimensionless potential vorticity anomalies become

$$q_1 = (\nabla^2 - \lambda^2)\psi_1 \quad (10)$$

for the EB model and

$$\begin{aligned} q_1 &= \nabla^2 \psi_1 + \frac{\lambda^2}{1+\delta} (\psi_2 - \psi_1), \\ q_2 &= \nabla^2 \psi_2 + \frac{\delta \lambda^2}{1+\delta} (\psi_1 - \psi_2), \end{aligned} \quad (11)$$

for the 2LQG model.

In the experiments discussed below, the basin is rectangular and the dimensionless model domain is $0 < x < 1$, $0 < y < 2$. The models are forced with a double-gyre pattern of Ekman suction,

$$w(y) = -\sin(\pi y), \quad 0 < y \leq 2. \quad (12)$$

The dimensionless parameters that appear in each of the models are δ_I , δ_M and the non-dimensional inverse baroclinic deformation radius, λ . In addition, the 2LQG model depends on the layer depth ratio δ . We define the Reynolds number for these models as the ratio

$$\frac{\delta_I^2}{\delta_M^3} = \frac{fW}{\beta H_1} \frac{L}{\nu} = \frac{fWL}{\beta H_1 \delta_j} \frac{\delta_j}{\nu}, \quad (13)$$

where $j = M$ or I .

In Sects. 4, 5 and 6, we explore the time-evolving singular values and singular vector structure in three different regimes of the wind-driven double-gyre circulation. The experiments are conducted with both the EB and 2LQG models in order to observe first, the behaviour of the first baroclinic mode alone, and then the effect of adding a barotropic mode. The models are spun up in an idealized rectangular ocean basin of dimension $L_x = 2048$ km and $L_y = 4096$ km in the meridional and zonal directions, respectively, and the characteristic width L is taken to be 2048 km. The upper layer depth H_1 , in both models, is set to 500 m for all the cases. The internal deformation radius L_D , is taken to be 40 km when modeling the steady and weakly aperiodic regimes, and 48 km for the strongly aperiodic regime. The Coriolis parameter f is 10^{-4}s^{-1} , β is $2 \times 10^{-11} \text{m}^{-1} \text{s}^{-1}$ and ρ_0 is 1000kg m^{-3} . W is taken to be $\tau_0/fL\rho_0$, which corresponds to applying a sinusoidal wind stress $\boldsymbol{\tau} = -\pi^{-1} \tau_0 \cos(\pi y)$, $0 < y < 2$.

The EB model is always run with no-slip lateral boundary conditions, while the 2LQG model uses free-slip boundaries for all but the steady-state case. For a domain of this size, higher Reynolds numbers result in an early separation of the WBC from the coast in the 2LQG model when no-slip boundaries are used. This is prevented by using free-slip boundary conditions. Bottom friction is negligible in these model runs. During the spin-up phase, which lasts 2500–4500 days in these experiments that starts from rest, we add a small, time-varying random perturbation to the wind in order to break the symmetry of the flow. Beyond spin-up, the models are forced by a steady symmetric wind field. In the 2LQG model, the ratio of layer depths δ , is 1/9. The viscosity and wind stress are varied to obtain different regimes of the flow.

The nonlinear forward model is similar to the one used by Holland (1978). The vorticity equations are discretized with second order finite differences and advanced in time with a second-order Runge-Kutta scheme. The Jacobian is discretized following Arakawa (1966). The grid is uniform with square mesh elements and a resolution of 129×257 . The time step is 0.1 non-dimensional units, which corresponds to 127 min and 50 s. The elliptic relations (11) are inverted for

the stream functions by first applying a linear transformation that yields elliptic equations for the barotropic and baroclinic components. The equation for the baroclinic stream function is split into two parts, an inhomogeneous equation with homogeneous boundary conditions and a homogeneous equation with inhomogeneous boundary conditions. The two elliptic problems with homogeneous boundary conditions are solved using a direct solver (one-dimensional sine-FFT followed by tridiagonal inversion). The remaining elliptic problem is solved once at the start of each run with a unit boundary condition, using a multi-grid solver.

3 Singular vectors

Singular vectors have a long history with implicit applications in fluid dynamics dating back to at least the work of Orr (1907). Ideas about the transient growth of perturbations governed by non-normal operators has received considerable attention in fluid dynamical studies of the transition to turbulence (Gustavsson, 1991; Trefethen et al., 1993). Atmospheric scientists have looked at singular vectors or non-normal instabilities as a way of understanding the growth of the errors in the forecasts (Lorenz, 1965; Palmer et al., 1998) or the transient growth of the disturbances (Farrell, 1984).

We adopt the notation that \mathbf{q} represents a column vector with elements that are the value of the potential vorticity at each successive interior grid point of the model. In the case of the two-layer model, values of the lower layer potential vorticity are listed after the upper layer potential vorticity values.

Both of our circulation models can be expressed as a generalized, nonlinear model (NLM) of the form

$$\frac{d\mathbf{q}}{dt} = N(\mathbf{q}, t). \quad (14)$$

By its definition, the state vector $\mathbf{q}(t)$ consists of the values of all of the prognostic variables at all of the grid points in the finite difference model. N represents the discretized form of the nonlinear governing equations.

We choose an inner product, (\mathbf{x}, \mathbf{y}) , between any two state vectors \mathbf{x} and \mathbf{y} . The associated norm is $\|\mathbf{x}\| := (\mathbf{x}, \mathbf{x})$, e.g. $\|\mathbf{x}\|$ may be the energy or enstrophy of the flow. The choice of norm dictates the quantity whose growth is maximized by the dominant singular vector. This has an implicit effect on the scale content of the initial and final forms of the singular vector (Palmer et al., 1998).

Given an initial condition, \mathbf{q}_0 , and a time interval $I_T := [0, T]$, integrating the NLM yields a trajectory

$$C_{\mathbf{q}_0} := \left\{ \hat{\mathbf{q}}(t) : \hat{\mathbf{q}} = \mathbf{q}_0; \frac{d\hat{\mathbf{q}}}{dt} = N(\hat{\mathbf{q}}, t), t \in I_T \right\}. \quad (15)$$

Linearizing about Equ. (14) provides a Forward Tangent Model (FTM) to the original nonlinear model along the trajectory $C_{\mathbf{q}_0}$, i.e.

$$\frac{d\mathbf{q}'}{dt} = M(\hat{\mathbf{q}}(t), t)\mathbf{q}'. \quad (16)$$

Integrating Eq. (16) over any finite interval $I_1 := [t_0, t_1]$, $0 \leq t_0 < t_1 \leq T$ contained in I_T , we obtain a linear map

$$\mathbf{q}'_1 = L(t_0, t_1)\mathbf{q}'_0, \quad \mathbf{q}'_0 \in H_{t_0}, \quad \mathbf{q}'_1 \in H_{t_1}, \quad (17)$$

from the Hilbert space (equipped with the norm defined above) of initial conditions at $t = t_0$, H_{t_0} , to the Hilbert space of final states at $t = t_1$, H_{t_1} .

We call L the *forward tangent propagator* and define an *adjoint propagator*, $L^* : H_{t_1} \rightarrow H_{t_0}$, by

$$(L^*\mathbf{x}, \mathbf{y}) = (\mathbf{x}, L\mathbf{y}) \quad \text{for all } \mathbf{x} \in H_{t_1}, \mathbf{y} \in H_{t_0}. \quad (18)$$

The *singular vectors*, $\{\mathbf{e}_i\}$, and *singular values*, $\{\sigma_i\}$ are defined to be the eigenvectors and eigenvalues of the linear Osledec operator, L^*L , which maps H_{t_0} to itself.

The forward nonlinear model, the forward tangent model, and the adjoint model are all readily implemented numerically. Note, for example, that the forward nonlinear model for the equivalent barotropic model may be written as

$$\begin{aligned} \frac{d\mathbf{q}}{dt} &= N(\mathbf{q}, t) = A\mathbf{q} + B\mathbf{p} + C(\mathbf{p}, \mathbf{q}) \\ &= A\mathbf{q} + BD^{-1}\mathbf{q} + C(D^{-1}\mathbf{q}, \mathbf{q}), \end{aligned} \quad (19)$$

where A , B , and D are linear difference operators (D is just the discretized Helmholtz operator), and C is a skew-symmetric bilinear form that corresponds to the discretization of the Jacobian.

We now discuss the interpretation of singular vectors. Let the singular values be indexed in order of decreasing size, $\sigma_1 > \sigma_2 > \dots$. Let the initial condition \mathbf{q}'_0 represent a *small* disturbance to the solution of the nonlinear model at time t_0 . If the interval I_1 is sufficiently short that the FTM, which is a linearization that *follows* the time-dependent trajectory of the nonlinear model, remains a good approximation for the evolution of this disturbance over I_1 , then the norm of the perturbation to the nonlinear model at time t_1 is approximately

$$\|\mathbf{q}'_1\| = (\mathbf{q}'_1, \mathbf{q}'_1) = (L\mathbf{q}'_0, L\mathbf{q}'_0) = (\mathbf{q}'_0, L^*L\mathbf{q}'_0). \quad (20)$$

Hansen and Smith (2000) discuss the relation between limits on the length of I_1 and the initial disturbance \mathbf{q}'_0 . Then

$$\max_{\mathbf{q}'_0} \left(\frac{\|\mathbf{q}'_1\|}{\|\mathbf{q}'_0\|} \right) = \sigma_1, \quad (21)$$

i.e. the maximum amplification of a small disturbance that can occur over the interval I_1 is given by the first singular value, σ_1 , and the spatial structure of the maximally amplified initial condition is given by the first singular vector, \mathbf{e}_1 . The shape of the disturbance into which this evolves at $t = t_1$ is given by $\mathbf{f}_1 = L\mathbf{e}_1$. In general, L is non-normal, \mathbf{e}_1 is not a scalar multiple of \mathbf{e}_1 , and \mathbf{e}_1 is not a normal mode.

The size of σ_1 provides an indirect measure of the fastest rate at which a trajectory perturbed a small distance from the original model trajectory $\hat{\mathbf{q}}(t)$, at t_0 , will diverge from the original trajectory when averaged over the interval I_1 . Hansen and Smith (2000) discuss the relation between limits

on the length of I_1 and the initial disturbance q'_0 . A related measure of the rapidity of the growth of the dominant singular vector is the time it takes for the singular vector to double, which has the advantage of being independent of the choice of I_1 . When considering transiently growing disturbances, neither of these completely characterizes the evolution of the singular vector, since there are typically multiple time scales involved, for example, the length of the period of growth and the inverse of the growth rate averaged over that period. One should remember that since both σ_1 and the doubling rate are properties of the “most rapidly” growing singular vector, they depend on the optimization time used. For example, if the optimization time is shortened, then σ_1 may increase. However, for the examples below, the structure of the leading singular vectors and their associated doubling times are smooth, and fairly weak functions of the optimization time over time scales characteristic of the ocean mesoscale (3–30 days).

The singular vectors and values have another interpretation. If we imagine a predictive numerical model of part of the ocean, the singular vectors and values describe how small errors in the state vector at time t_0 evolve over the interval I_1 . If the initial error covariance matrix is isotropic, then the vectors Le_i are the principle axes of the error covariance matrix at $t = t_1$, and the singular values σ_i describe the amount of extension or contraction along each principle axis. Conversely, if we wish to have an isotropic error covariance matrix at time t_1 , then we must ensure that the lengths of the principle axes, e_i of the initial error covariance matrix are proportional to $1/\sigma_i$. This identifies the “directions” in which it is most important to minimize initialization errors if we are to control the prediction errors. Since q is the state vector of an ocean general circulation model, each singular vector corresponds to a particular spatial pattern of the prognostic variables.

Yet another geometric interpretation of the singular vectors is the following and is illustrated in Fig. 1. If we take a particular point q_0 on a nonlinear trajectory and imagine a hyperspherical ball of initial conditions centered on q_0 (for example, a cloud of initial conditions representative of measurement errors), then while the linear approximation remains reasonable, this cluster of initial conditions will evolve into a hyperellipsoid with axes corresponding to the evolved forms f of the singular vectors. These are mutually orthogonal (or can be made so in the event of eigenvalues with a multiplicity greater than 1), since they are eigenvectors of the normal operator LL^* . The expansion of the ellipsoid in some directions gives an indication of the degree to which trajectories diverge. Note that an extension of the ellipsoid parallel to the tangent to the nonlinear trajectory at the final time t_1 represents a different sort of error than an extension perpendicular to the final tangent direction. The first is really a phase error and represents an error in predicting when the flow will pass through the point $q(t_1)$ on the nonlinear trajectory. The second type of error represents an error in the predicted *structure* of the final state.

It is important to remember that growing singular vectors,

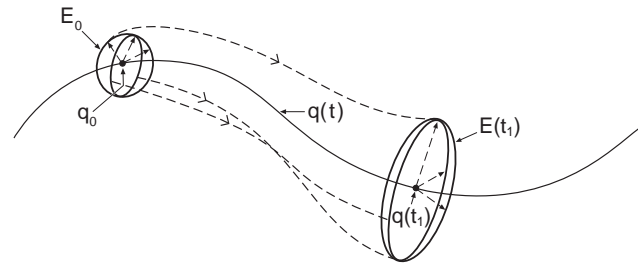


Fig. 1. In this geometric interpretation of the singular vectors, a particular point q_0 on a nonlinear trajectory is surrounded by a hyperspherical ball or cloud of possible initial conditions (such as those arising from measurement errors) centered on q_0 . While the linear approximation remains reasonable, this cluster of initial conditions will evolve into a hyperellipsoid with (mutually orthogonal) principal axes corresponding to the evolved forms f of the singular vectors. The expansion of the ellipsoid in some directions gives an indication of the degree to which the trajectories diverge.

those with singular values are greater than 1, can exist for a combination of reasons. One mechanism that can give rise to an amplifying disturbance is a dynamical instability. For example, suppose that the operator L is stationary and *normal*, then the eigenvectors are orthogonal and the singular vectors are parallel to the eigenvectors. Consider the simple example of an unstable, two-dimensional system with one growing eigenvector and one decaying eigenvector, as shown in Fig. 2a. Any disturbance that is sufficiently close to being parallel to the unstable direction will grow as a result of that instability. When the linearized system represented by the operator L is non-normal, the eigenvectors of L are typically non-orthogonal. Again, considering an example in which L is stationary and two-dimensional demonstrates how a dynamical instability represented by a growing eigenvector can lead to the growth of a disturbance that is initially almost parallel to it (Fig. 2b). However, one of the somewhat counter-intuitive aspects of non-normal systems that should be kept in mind is that even for a stable system, there can exist disturbances which exhibit transient growth. This can occur when two decaying eigenvectors of the non-normal operator L are non-orthogonal and have different eigenvalues, as demonstrated in Fig. 2c.

When computing singular vectors, the choice of norm is dictated, in part, by their intended use. Here, we are interested in the differences between trajectories of the phase space of the model. Potential vorticity is the natural dynamical variable in the QG models and its grid-point values are chosen as the coordinates for this phase space. A natural choice of metric in this space is thus enstrophy, and the enstrophy norm is used in the singular vector calculations. Since the potential vorticity of the flow is the only prognostic quasi-geostrophics variable in a closed domain with properly posed boundary conditions, all non-trivial choices of a norm will lead, in one way or another, to singular vectors that rearrange the potential vorticity field. However, two other typical

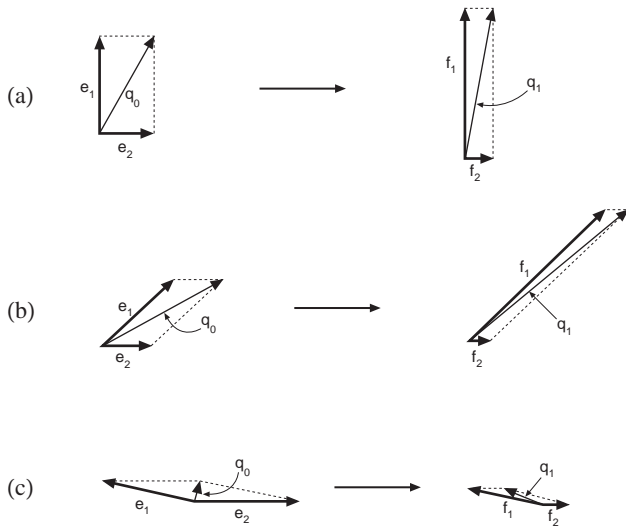


Fig. 2. In each panel, two eigenvectors of a stationary linear operator, L , are shown with bold lines. A third vector q_0 , corresponding to a disturbance to the underlying system, is shown by a thin line. The initial (non-normalized) eigenvectors are denoted by e_i and their evolved forms (after being operated on by L) are denoted by f_i . The evolved form of q_0 is q_1 . The following three cases are depicted: (a) L normal, with one unstable and one stable eigenvector; (b) L non-normal, with one unstable and one stable eigenvector; (c) L non-normal, with two stable eigenvectors with unequal eigenvalues.

choices of norm, the stream function and the energy norms, tend to integrate the effects of the rearrangements of potential vorticity in different parts of the flow.

In our numerical calculations of singular vectors, the tangent model used is a linearized form of the nonlinear forward model. The linearization is an approximation to the time-dependent trajectory of the nonlinear model constructed by piecewise linear interpolation between points on the exact trajectory that are spaced 10 time steps apart. The adjoint is the exact (to within machine rounding error) discrete adjoint of the discrete tangent model. The singular vectors of the system are obtained by finding eigenvectors of the Oseledec operator using the Lanczos algorithm.

4 Singular vectors of steady circulations

In this section, we examine the singular vectors of steady, double-gyre circulations. For $\nu = 1000 \text{ m}^2 \text{ s}^{-1}$, $L_D = 40 \text{ km}$, a wind stress intensity of $\tau_0 = 0.11 \text{ Nm}^{-2}$, and the existence of no-slip boundary conditions, both the EB and 2LQG models possess a stable, steady-state, double-gyre circulation. Since the same upper layer depth is used in both models, their upper layer circulations, shown in Fig. 3, are identical. Perturbations to the steady state evolve differently in the two models on account of their different vertical structures. In the EB model, a small perturbation can exchange

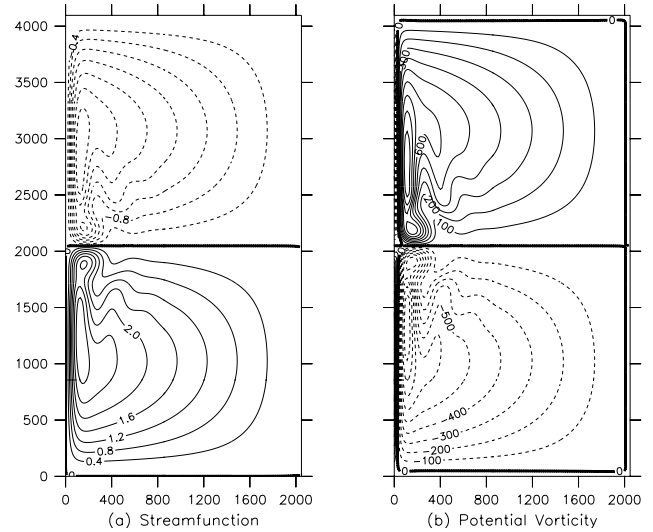


Fig. 3. Steady-state value of the upper layer (a) stream function and (b) potential velocity for the case with $\nu = 1000 \text{ m}^2 \text{ s}^{-1}$, $L_D = 40 \text{ km}$, $\tau_0 = 0.11 \text{ Nm}^{-2}$, and no-slip boundary conditions. Both the EB and 2LQG model upper layers have identical steady states.

energy with the background flow only through the barotropic energy conversion process associated with the rate of working of the horizontal Reynolds stress on the background momentum gradient (Pedlosky, 1987). The 2LQG model, on the other hand, can also simulate a horizontal heat flux. In this model, a small perturbation may exchange energy with the background flow through both barotropic and baroclinic energy conversion terms. We will attempt to identify physical mechanisms associated with the growth of optimal perturbations (singular vectors) by initializing the models with a singular vector and allowing this perturbation to evolve linearly. We will then compare the initial and evolved states of the perturbation, and examine the spatial pattern of energy conversion between the perturbation and background flow.

As was noted in Sect. 3, it is not a contradiction that a *stable* flow (in the mathematical sense of asymptotic stability) should possess *growing* finite-time singular vectors. Due to the shears present in the steady-state flow, small disturbances with an appropriately chosen spatial distribution can extract energy from the local horizontal or vertical shear. As the locally growing part of the perturbation grows, it is also advected through the region where its phase structure favors the extraction of energy from the background flow. Once outside this region, growth ceases and dissipation acts to dampen the local disturbance, while the adverse shear may extract energy from the disturbance. Sustained growth (as would be seen if the disturbance were a growing normal mode) can only occur if (a) the disturbance is eventually advected back into the unstable part of the background flow, (b) some component of the disturbance re-entering the unstable region has the correct phase structure to extract energy from the background flow, and (c) the growth in enstrophy experienced by

the disturbance as it passes through the unstable region is greater than the decay experienced during the phase in which the disturbance is being advected away from and then back into the unstable region. From the perspective of trajectories in phase space, the case in which a stable flow possesses growing finite-time singular vectors corresponds to a situation in which there exist some directions in which nearby trajectories are locally diverging from the fiducial trajectory (the point in phase space that corresponds to the steady state). However, eventually these trajectories curve back towards the fiducial trajectory and asymptote to it.

We begin by examining the singular vectors of the stable steady state in the two models. The singular vectors are calculated to optimize enstrophy growth over a period of 10 time units, i.e. approximately 8.9 days. Figures 4 and 5 show, in an enlarged view of the region surrounding the separation point of the jet, the first or dominant singular vector, i.e. the transient disturbance with the largest amplification rate, for the EB and 2LQG models, respectively. The left panels show the singular vector structure or initial potential vorticity and stream function prescribed as a perturbation, the middle panels show their linearly evolved states at $t = 10$, and the right-most panels show the mean energy conversion rates over the period $t = 10$, as defined in the Appendix of Berloff and Meacham (1998). In both models, the first singular vector, which has the largest singular value, corresponds to the latitudinal variation of the point at which the mid-latitude jet separates from the western boundary. The initial structure of this perturbation has a relatively large spatial scale and is anti-symmetric about the middle latitude of the basin. Its largest amplitude occurs straddling this line, over towards the western boundary. Since the anomaly has the same sign on both sides of the middle latitude, its effect is to strengthen one of the inertial gyre recirculations and weaken the other. This intensification of circulation in one half-basin and the weakening in the other, strengthens the WBC on one side of the separation point and weakens it on the other. When superimposed on the basic state, i.e. the steady solution in Fig. 3, the result is a meridional displacement of the separation point into the half-basin with the weakened recirculation. Evidence of the deceleration of one WBC and the acceleration of the other may be seen in the final state of the singular vector, in which a thin band of anomalous potential vorticity, symmetric about the mid-latitude of the basin, appears adjacent to the western boundary. This is due to the change in shear stress and hence, the vorticity in the viscous sub-layer adjacent to the western boundary. The acceleration of one boundary current in one direction and the deceleration of the second boundary current flowing in the opposite direction give vorticity anomalies of the same sign adjacent to the boundary.

The final state of the dominant singular vector also contains two zonally elongated extrema of potential vorticity of the same sign on either side of the axis of the jet. When combined with the strong shears that are the poleward and equatorward flanks of the mid-latitude jet, these strengthen one and weaken the other. To leading order, they represent

a meridional displacement of the axis of the jet within a few hundred kilometers of the western boundary. As the separation point moves, advection along the jet carries the knowledge of the position of the separation point into the domain. Zonal flow speeds in the shear maxima off the axis of the jet are roughly 0.15 m/s. In 8.9 days, water parcels moving at this speed will travel approximately 115 km. This is similar to the penetration scale of the vorticity extrema on the flanks of the jet. Note that while the meridional displacement of the separation point and jet axis is proportional to the amplitude of the disturbance, which is arbitrary in this linear theory, the zonal penetration of the influence of the displacement of the separation point is proportional to the strength of the zonal flow of the basic state.

While the structure and evolution of the dominant singular vector are similar in both the reduced gravity and two-layer cases, there are some differences. Most notable is the fact that in the two-layer case, the perturbation has a larger zonal scale, which is larger than its meridional scale. The large-scale component has a significant barotropic part. The structure of the dominant singular vector for the two-layer problem can be thought of, somewhat crudely, as a disturbance similar to that seen in the reduced gravity problem, plus a barotropic Rossby wave, which has a larger zonal than meridional scale and hence, has a westward group velocity. It propagates rapidly westward to the western boundary where it reflects as a Rossby wave of short zonal scale and eastward group velocity. Since the magnitude of the zonal group velocity of the eastward wave is much less than that of the westward wave, the reflected wave has a significantly larger amplitude. For times less than half the period of the wave, its effect on the WBC is to reinforce the effect produced by the baroclinic disturbance, slowing one of the WBCs while accelerating the other. While the QG model with a rigid-lid does contain a representation of a baroclinic Kelvin wave, albeit one with an infinite phase speed, it does not admit a barotropic Kelvin wave and so no such wave is induced by the incident Rossby wave. Even if the rigid-lid approximation were relaxed, the amplitude of the barotropic Kelvin wave would be weak.

In the barotropic and baroclinic energy conversion terms of Figs. 4 and 5, the positive values near the boundary indicate that over the period $t = 10$, the initial perturbation extracts energy from the mean state. The growth of the perturbation initially consists of a strong symmetric potential vorticity anomaly in the region of the WBC near the separation point. Since the flow is actually stable, this disturbance would eventually start to lose energy to the background flow if integrated further. If integrated over a period long enough to re-establish a steady state, then the sum of the growth and decay would amount to zero.

The singular vector corresponding to the second largest distinct singular value is anti-symmetric with more of its structure distributed away from the jet axis, while that corresponding to the third is similar to the first, which is symmetric about the jet axis (Fig. 6).

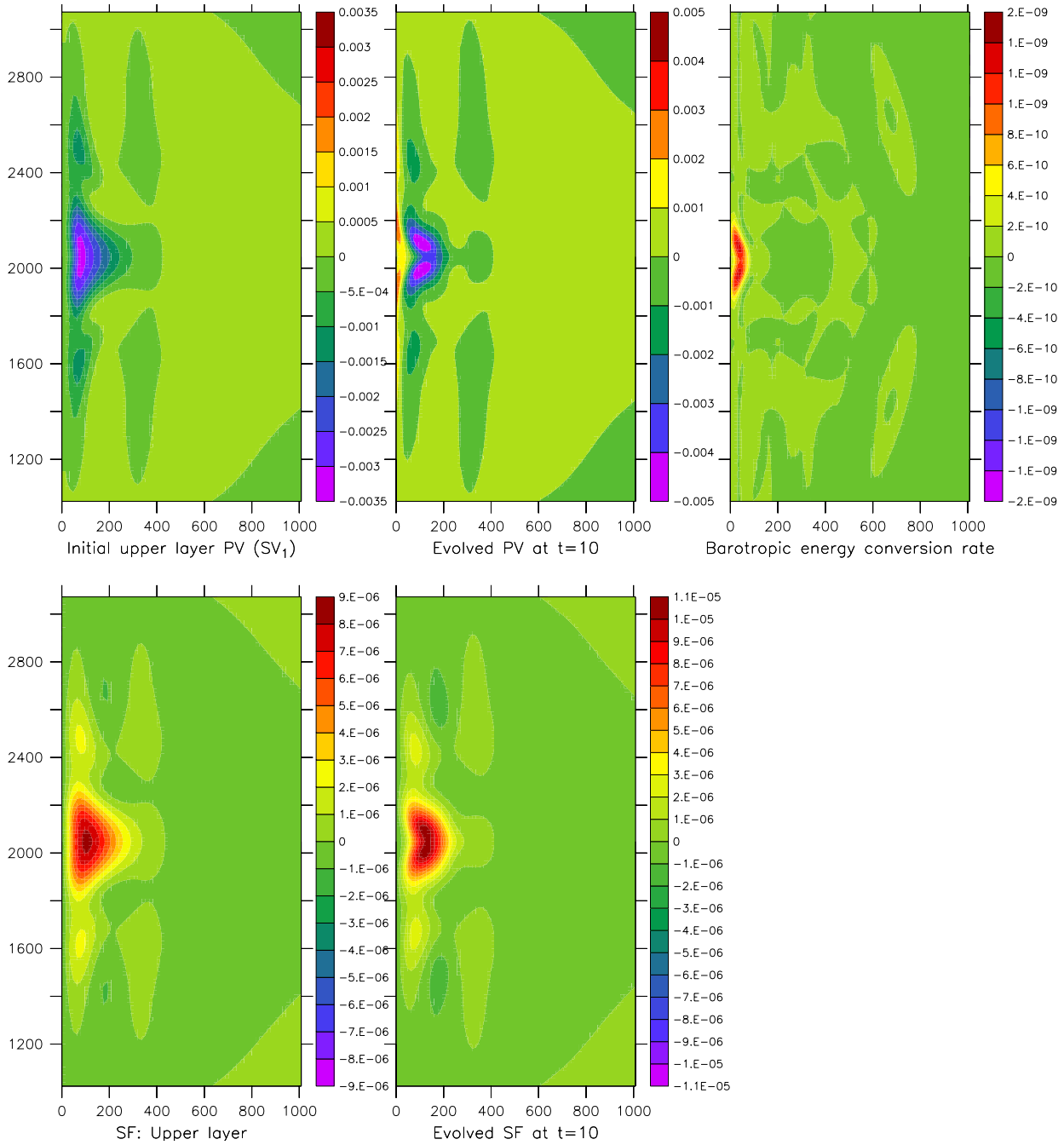


Fig. 4. The first singular vector corresponding to the enstrophy norm computed for the steady state in the EB model using an integration time of 10 units (approximately 8.9 days). The figures show an enlarged view of the western half of the domain and only half of the northern and southern extent. The left panels show the singular vector structure or the initial potential vorticity and stream function prescribed as a perturbation, the middle panels show their linearly evolved states at $t = 10$ (8.9 days), and the right-most panels show the mean (over the period $t = 10$) of the energy conversion rates defined in the Appendix of Berloff and Meacham (1998).

5 Singular vectors of weakly aperiodic (irregularly vacillating) flows

Reducing the eddy viscosity to $\nu = 500 \text{ m}^2 \text{ s}^{-1}$ changes the solution of the wind-driven double-gyre model described above, from a steady state to one that varies aperiodically between states of “high” and “low” energy in a relaxation oscillation.

To attain this state, we spin up the EB and 2LQG models for 12 and 18 years, respectively, with a small time varying random perturbation to the wind stress. Once spun up, the wind stress is held symmetric and steady, and the model solution vacillates between different states due to its own natural internal variability. A time series of the kinetic energy of the upper layer shows the build up of energy that corre-

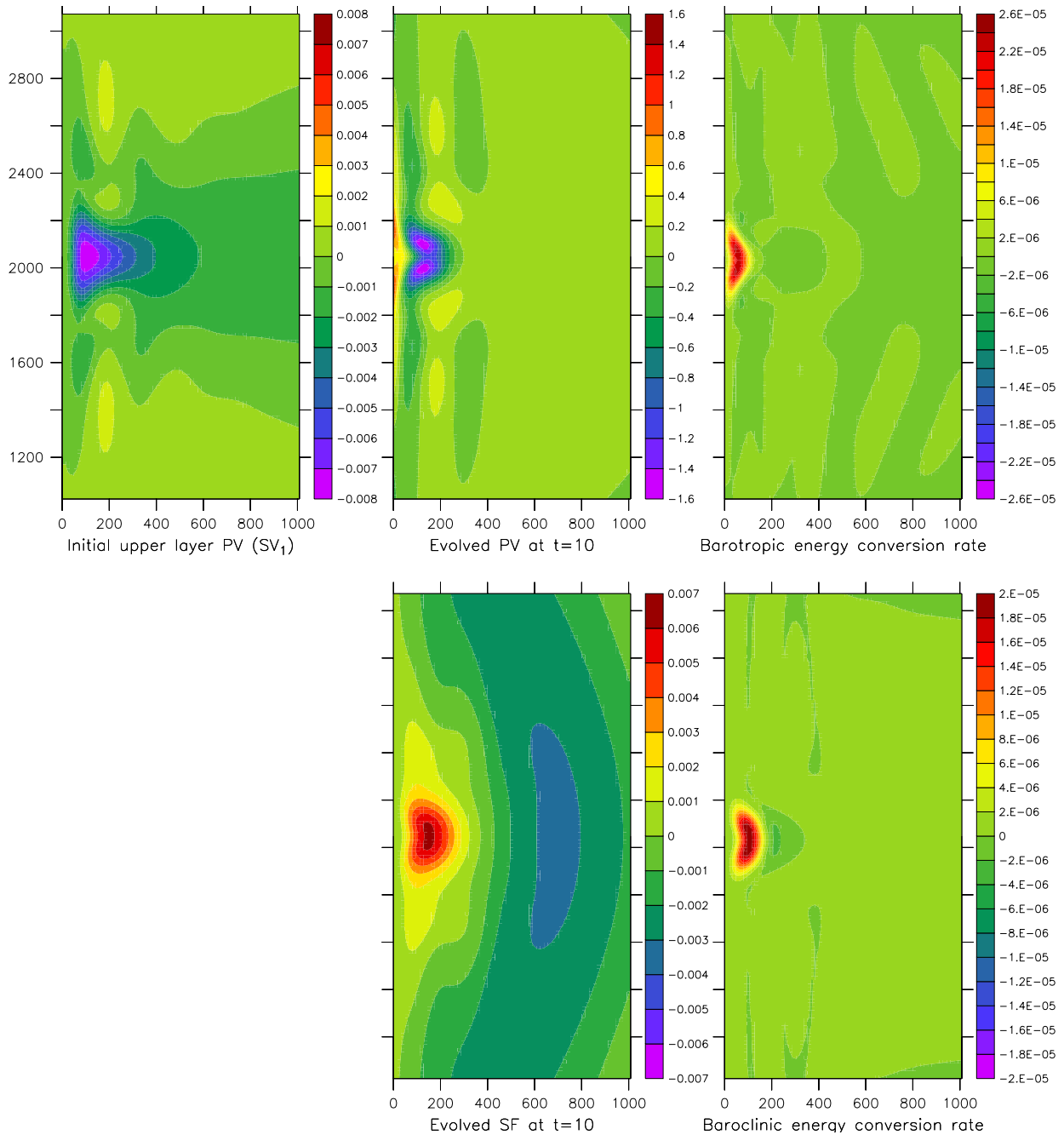


Fig. 5. Same as Fig. 4, but for the upper layer of the 2LQG model.

sponds to the increasing extension of the zonal jet, which then breaks up catastrophically, resulting in a sudden drop in the kinetic energy. Figures 7 and 8 show snapshots of the upper layer stream function in the high and low energy states for the EB and 2LQG models, respectively. The high energy state, in the left panels of Figs. 7 and 8, are characterized by an intense jet that penetrates into the basin interior with strong northern and southern inertial recirculations. The low energy states, seen in the right panels, are characterized by a “retracted” jet whose structure has been broken by instabil-

ities giving rise to smaller recirculations localized near the western boundary. In the EB model, the mid-latitude jet exhibits a greater tendency to fold back on itself. Baroclinic eddies in the 2LQG model result in a higher level of mesoscale “noise” in the energy (Fig. 10), as compared to the EB model (Fig. 9). The breakup of the extended jet in the 2LQG model occurs with the formation of baroclinic eddies that dissipate energy more effectively, and consequently, the drop in energy in the 2LQG model is rather more dramatic than in the EB model (see Figs. 9 and 10). The vacillation time scales

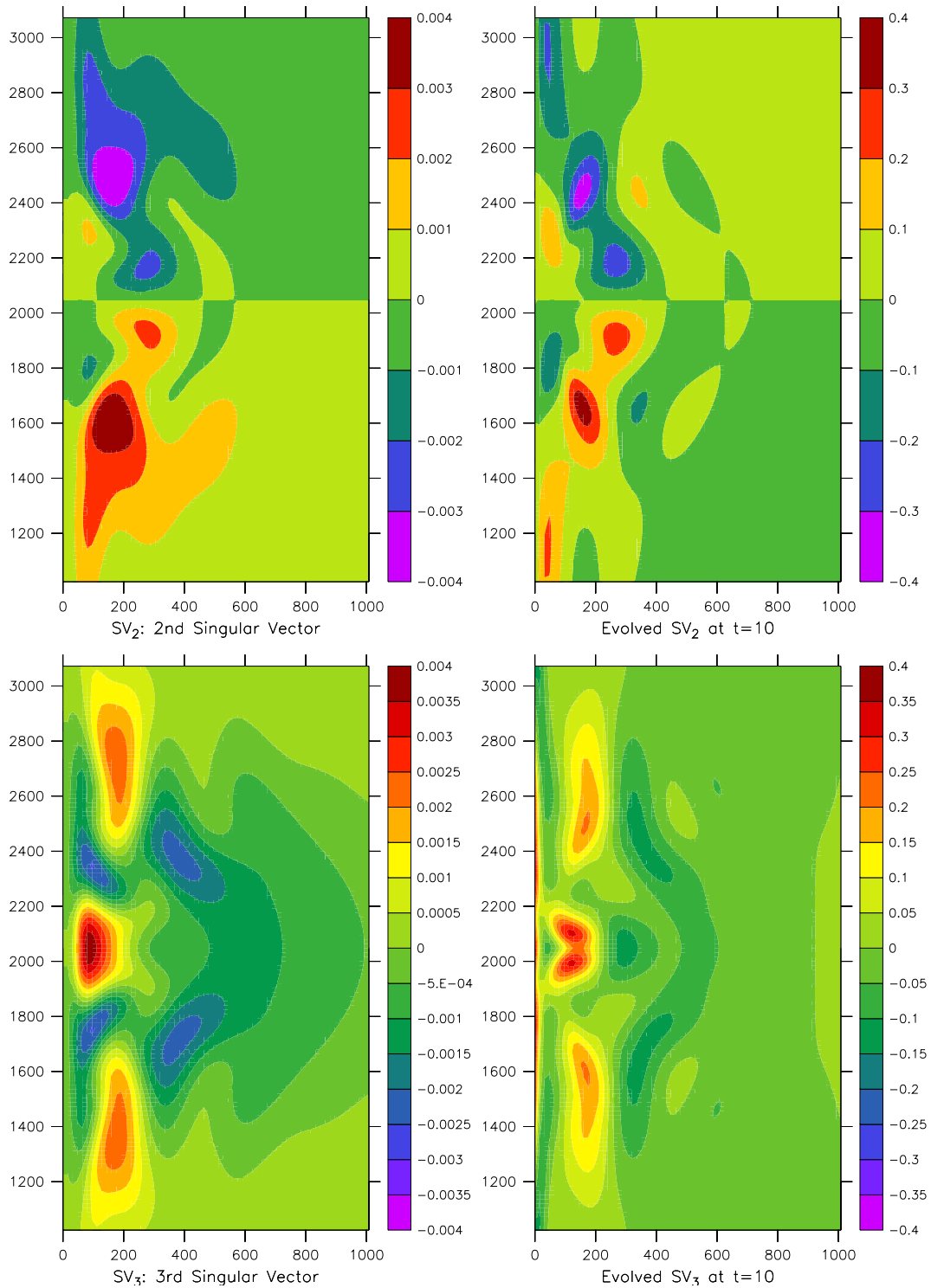


Fig. 6. The left panels show the structure of the 2nd and 3rd singular vectors, i.e. singular vectors corresponding to the 2nd and 3rd largest unique singular values, from the 2LQG model. The right panels show the evolved state of these singular vectors when the domain is initialized with these potential vorticity perturbations and allowed to evolve linearly for $t = 10$ (8.9 days). Once again, the region of interest around the jet separation point is enlarged.

for the EB and 2LQG flows are approximately 10 and 20 years, respectively. These high and low energy states correspond to similar states observed in the simulations of Mc-

Calpin and Haidvogel (1996), Primeau (1999) and Meacham (2000), and are indicative of long-time internal variabilities of the wind-driven gyres.

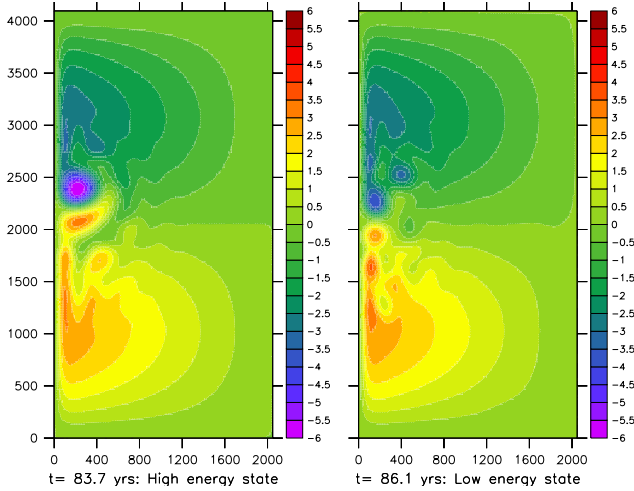


Fig. 7. Snapshots of the EB model stream function in high and low energy states of the weakly aperiodic or irregularly vacillating flow regime attained when $\nu = 500 \text{ m}^2 \text{ s}^{-1}$. The high energy state in the left panel is characterized by the increased penetration of the mid-latitude jet into the basin interior, while the low energy state seen in the right panel is characterized by a retracted and less energetic jet.

The question is whether the singular values and singular vector structure reflect the large-scale change in the state of the evolving flow field. Could they also be viewed as precursors to these changes? To address these issues, we compute the singular values and vectors, once again maximizing the enstrophy norm over a period $t = 10$ (8.9 days), at intervals of $t = 100$ following the evolution of the flow. Figure 9 shows a time series of the first three singular values and the total kinetic energy for the EB model. The upper panel shows the original time series, and the lower panel shows the time evolution smoothed with a running mean over a period of roughly 1.6 years. The first three singular values are highly correlated with the kinetic energy, with sharp increases in the singular values preceding sharp decreases in the kinetic energy, and sharp decreases in the singular values preceding a smoother successive increase in the kinetic energy. The singular value behaviour is thus a precursor of the transition from high to low energy states and *vice versa*. The transition from the high to the low energy state is rather abrupt, while the opposite transition is smooth and gradual. The precursor of a transition in the flow regime is an abrupt change in the slope of the time evolution of the singular value. A sharp increase in the slope always precedes the successive collapse of the kinetic energy. The successive sharp decrease in the singular value with a strongly negative slope is a precursor of the consequent increase in kinetic energy, at which time the singular value begins to grow again until the next transition to the low energy state.

Preliminary experiments with the 2LQG model showed that there was no resemblance between the time series of singular values and kinetic energy, since with no-slip boundary conditions, the singular vector structure is dominated by the

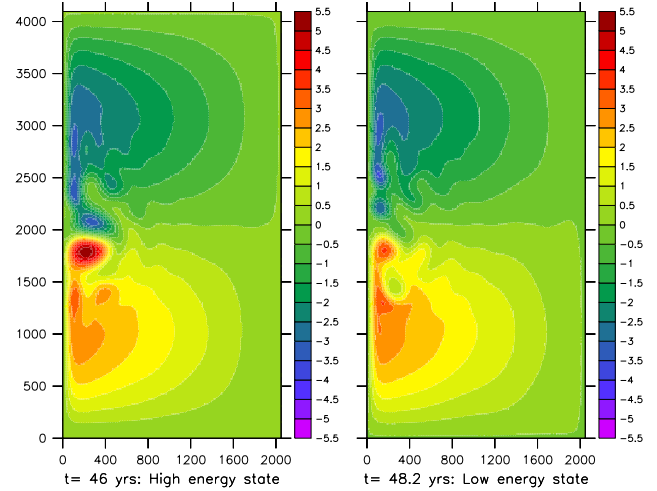


Fig. 8. Same as Fig. 7, but for the upper layer of the 2LQG model.

boundary adjustment in the lower layer of the model. In order to eliminate the effect of the boundaries, we only consider the interior of the domain, leaving out a buffer region (arbitrarily chosen to be 9 grid points wide) along the boundary. Formally, this is done by redefining $\| \mathbf{q}'_1 \|$ in Eq. (20) as

$$\| \mathbf{q}'_1 \| = (\mathbf{q}'_1, G \mathbf{q}'_1), \quad (22)$$

where G is a diagonal matrix with 1's and 0's on its diagonal. The 0's are situated in order to zero out the near-boundary grid point values of \mathbf{q} upon multiplication. With this modification, we begin to see a large correspondence between the time series of the dominant singular values and the kinetic energy. Figure 10 shows a time series of the 3 largest singular values. The time series is smoothed by a running mean with a window of $t = 500$ or 1.2 years to filter the very high frequencies as the singular values show much greater high frequency variability than in the EB case. All three singular values shown exhibit a change in their value corresponding to the change in the large-scale state of the flow, but the second shows the largest change in correspondence. The predictive character, i.e. the increase in slope or the rate of change in the singular value prior to the break up of the extended jet, is not as clear as in the EB case.

The singular vectors are constantly changing as the flow evolves. But the structure of the first, second and third singular vectors in this weakly periodic state are continuations of the structure of the respective singular vectors in the steady state. The first singular vector from the 2LQG model has a larger zonal extent than that from the EB model, but the size of the evolved structures are comparable. As in the steady state, this singular vector is associated with the north-south migration of the separation point.

To explore the extent of the parameter range in which the singular value maintains its predictive capability in the case of the EB model, we have explored the case with a reduced eddy viscosity coefficient $\nu = 350 \text{ m}^2 \text{ s}^{-1}$. Figure 11 shows

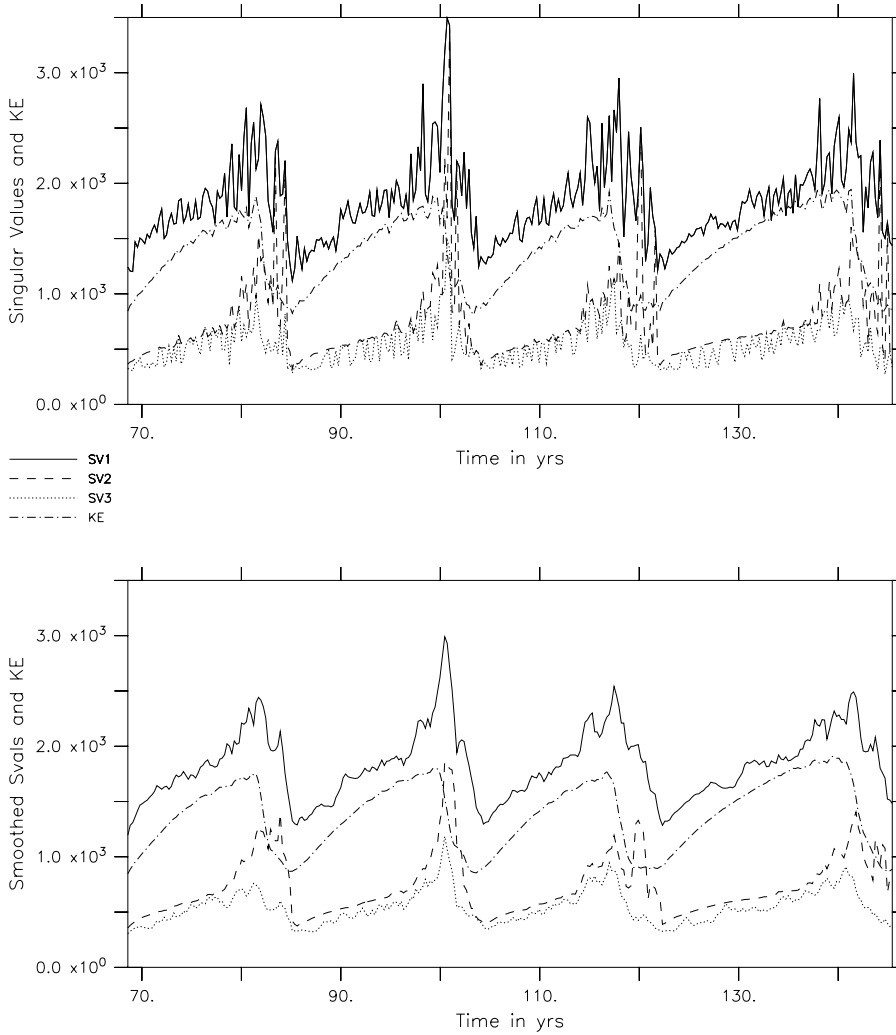


Fig. 9. Time series of total kinetic energy (in arbitrary, non-dimensional units) and the first three singular values of the EB model in the weakly aperiodic regime with $\nu = 500 \text{ m}^2 \text{ s}^{-1}$. The upper panel shows the original time series, while the lower panel shows the time series smoothed with a running mean over a period of roughly 1.6 years.

the analogous time series of the first three singular values evaluated as discussed above, together with the corresponding evolution of the kinetic energy for this reduced viscosity case. The upper panel shows again the original time series, and the lower panel shows the evolutions smoothed over a period of about 3.6 years. The period of the vacillation cycle has now increased to roughly 20 years. Both the singular values and the kinetic energy show much more vigorous high energy fluctuations, due to the more intense barotropic instability allowed by the reduced viscosity. Nevertheless, the singular values still have a predictive capability, as is apparent in the smoothed time series shown in the lower panel of Fig. 11. Again, the sharp change in the slope of the singular value evolution is a precursor of the transition in the flow regime, now characterized by greater changes in the energy levels.

Other indices of the large-scale state of the flow, such as the WBC transports and the crossing of the zero potential vorticity line, are also explored in the EB case. We estimate the WBC transports to be the difference in the stream function between the grid point $i = 10$ and the boundary for

sections that are 40 grid points north and south of the mid-latitude jet axis. In Fig. 12 we plot these WBC transports, where the northern transport is positive, and the difference between northern and southern WBC transports is indicative of the gyre asymmetry. We also plot the migration of the zero potential velocity line or jet axis just interior of the boundary (at $i = 2$) from the mid-axis of the domain. Both of these indices track the singular values and KE of the flow. However, they show that the vacillations are not symmetric. The jet axis near the separation point is gradually pushed northward by a growing recirculation region just south of the jet (see Fig. 7). This continues until the recirculating region collapses and the jet suddenly whips back in a southern direction. This abrupt change in jet position from north to south is coincident with a surge in the northern WBC transport and the attainment of maximum KE (see Figs. 11 and 12). Earlier experiments have shown that over long integration periods, the flow will also, at times, make a transition into the opposite phase where the jet will be forced southward and then whip back in a northern direction with a surge in the southern WBC.

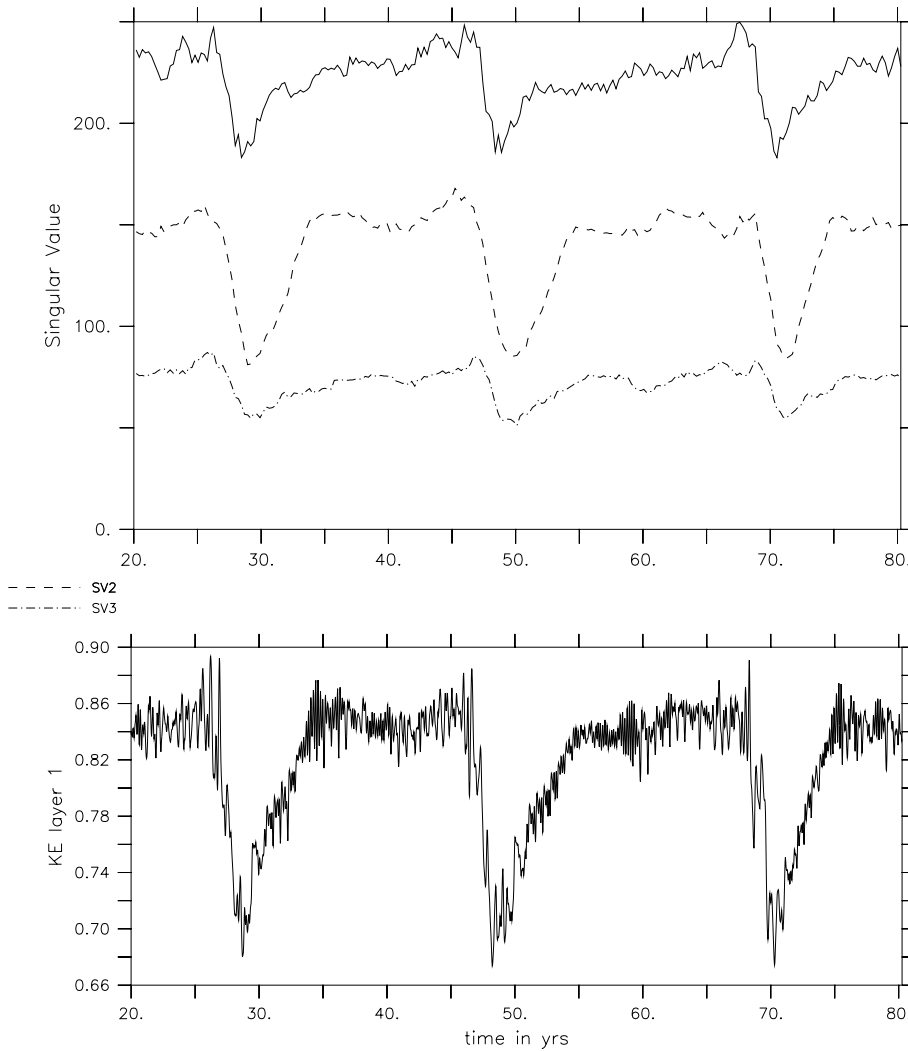


Fig. 10. Time series of the first three singular values (upper panel) and total kinetic energy (in arbitrary non-dimensional units) of the 2LQG model in the weakly aperiodic regime. The time series of the singular values was originally very noisy and, therefore, is smoothed by a running mean with a window of $t = 500$ or 1.2 years to filter the high frequencies.

6 Strongly aperiodic flows

When we move to more strongly aperiodic flows, the high degree of correlation between the behaviour of the singular values and the evolution of the structure of the large-scale flow disappears. Figure 13 shows the smoothed time series of the upper layer kinetic energy and the first three singular values for a run of the 2LQG model with $\nu = 100 \text{ m}^2 \text{ s}^{-1}$, the deformation radius L_D set to 48 km, and the wind stress intensity $\tau_0 = 0.05 \text{ Nm}^{-2}$. Significant variations in the magnitudes of the singular values can be seen. There is coherence between the time series of the three dominant singular values themselves, but no significant coherence between any of the singular values and the basin integrated kinetic energy of the upper layer flow. There is a similar lack of coherence between the time series of the dominant singular vectors and other integral measures of the flow, such as the WBC transport (not shown).

The reason for the lack of a strong correlation between the singular values and time series representing the large-scale spatial structure of the flow lies in the character of the singu-

lar vectors. In the strongly chaotic regime, there are a considerable number of mesoscale eddies in the flow, as well as strong meanders in the WBC extension. Much of the energy extracted by the dominant singular vectors as they grow comes from the intensification of perturbations in the regions of strong shears associated with these mesoscale phenomena, and the evolved forms of the singular vectors typically have large amplitudes near one or more of the mesoscale features. When the evolved singular vectors are assigned an arbitrary amplitude and superimposed on the unperturbed trajectory, they frequently correspond to displacements of one or more of the strong mesoscale features present.

As one moves from the regime of steady, periodic or weakly aperiodic solutions to that of the strongly chaotic solutions, the physics underlying the growth of the dominant singular vectors changes. The generation of the changes in the separation point and meridional displacement of the WBC extension is now supplemented by the displacement or stretching of strong meanders and mesoscale eddies as perturbations grow transiently in the strong shears adjacent to these features. The nature of the dominant singular vec-

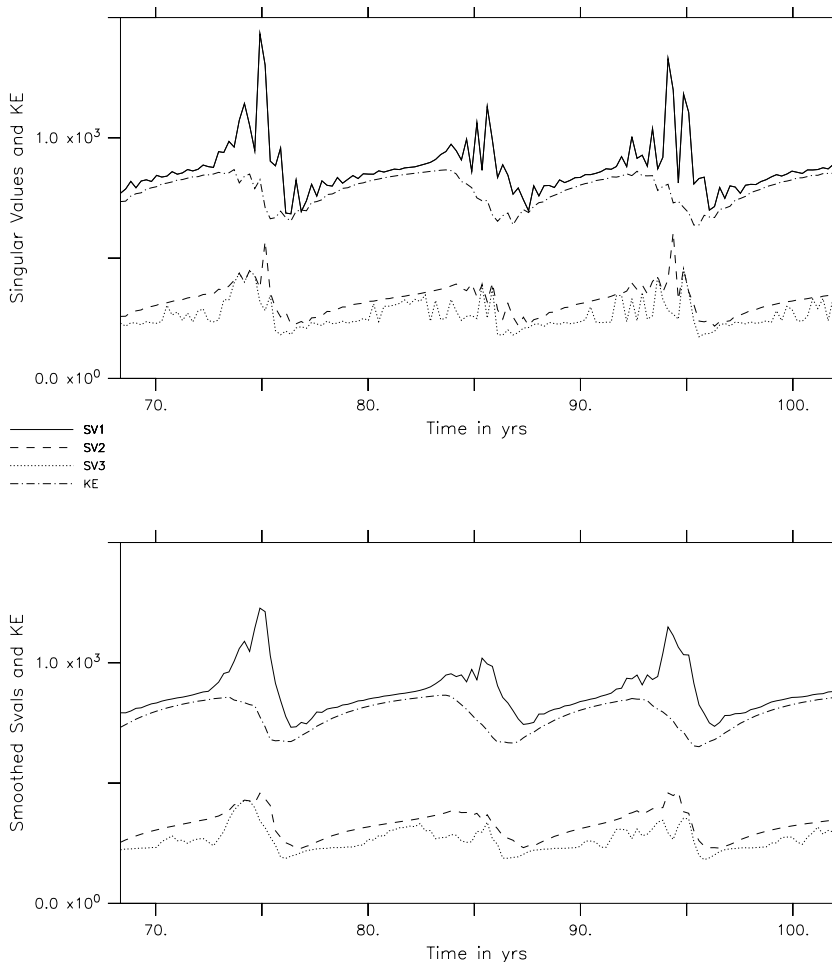


Fig. 11. Same as Fig. 9, but with $\nu = 350 \text{ m}^2 \text{ s}^{-1}$.

tors and the sizes of their associated singular values depend on relatively localized structures in the flow. As they grow, they produce localized changes to the flow (Moore and Mariano, 1999). This high degree of locality implies that the forecasting problem for flows in the strongly chaotic regime is both simpler and more difficult than in the weakly aperiodic regime. On the one hand, if the flow is to be predicted with a high level of accuracy over the whole domain, then all of these local “instabilities” must be resolved which, for an assimilative forecasting scheme, implies gathering a lot of data. On the other hand, it also implies that for much of the time, the short-term behaviour of the flow in a limited region will tend to be influenced more strongly by local processes rather than by remote ones, so that observations concentrated in a limited area around the region of interest should be more relevant to the forecasts in that region than the observations made further away. The obvious exception is close to the western boundary, where a significant signal can be associated with the reflection of large-scale barotropic Rossby waves. Observations in the interior of the basin would probably be needed to accurately include the effects of such phenomena in a forecast model for the flow adjacent to the boundary. The implication is that the variability in the

separation point of the WBCs, when relatively unconstrained by topography (e.g. off the east coast of South America), may be a more challenging problem than predicting the evolution of meanders in the Gulf Stream.

7 Summary and discussion

In this work, we briefly examined the structure of the dominant singular vectors of simple models of the wind-driven circulation and the way in which the associated singular values vary with the large-scale circulation. The main motivation comes from the information that the singular vectors contain the local rates of divergences of the trajectories in phase space and hence, the speed with which small errors in the initial or analyzed field of a forecast model will grow.

The main points that we would like to emphasize here are:

1. In time-dependent flows, the singular values, which reflect the rate of growth in the errors, and hence, the predictability of the flow, is very dependent on the instantaneous state of the flow.
2. When the Reynolds number of the modeled circulation is low and the time dependence of the flow is weak, the

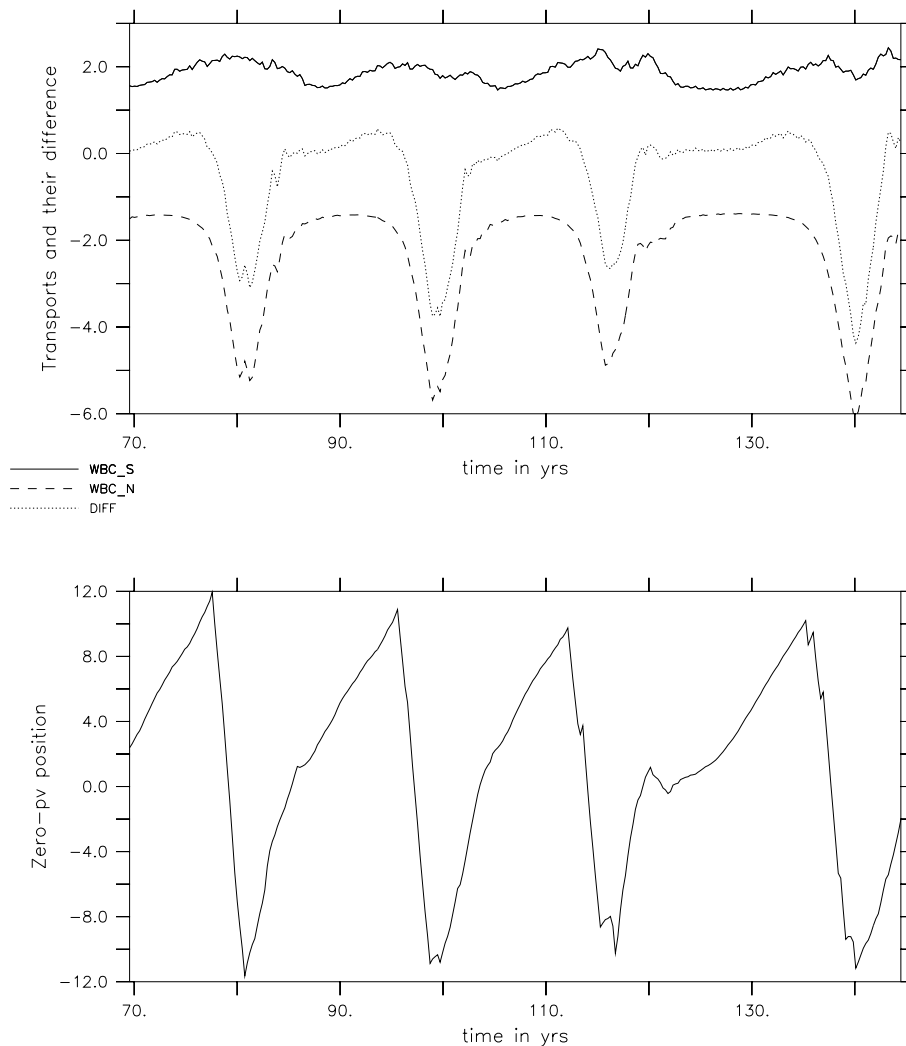


Fig. 12. Time series of the WBC transports (northward positive) and the zero potential vorticity crossing for the EB model in the weakly aperiodic regime with $\nu = 350 \text{ m}^2 \text{ s}^{-1}$. The upper panel shows the southern WBC transport (solid line with positive values), the northern WBC transport (dashed line with negative values) and the difference between the two. These transports are computed as the stream function difference between the points $i=10$ and 1, at sections that are 40 grid points north and south of the mid-latitudinal axis. The lower panel shows the north and south migration of the zero potential vorticity line (i.e. the jet axis) in grid points, just inside of the western boundary (at $i=2$). We observe an asymmetry in the vacillations. The jet axis near the separation point gradually migrates northward and then suddenly whips back in a southern direction. This abrupt change in jet position from north to south is coincident with a surge in the northern WBC transport.

singular vectors are relatively large-scale and the associated variability of the singular values is sensitive to simple measures of the large-scale flow. In the reduced gravity model, changes in the dominant singular values also herald large and relatively abrupt changes in the structure of the large-scale flow.

3. When the Reynolds number is high, local instabilities of mesoscale structures, similar to those examined by Moore and Mariano (1999), become significant contributors to the dominant singular vectors. Larger scale processes remain important contributors to phenomena, such as variability in the separation point of the WBC extension.

These results have a number of implications for the design of assimilative ocean forecasting systems. If one of the goals of the forecast system is to predict the position of the strong front associated with a WBC extension, then a significant amount of local data will be needed to accurately predict the evolution of meanders, ring genesis and the evolution of detached rings. Given that the singular values associated

with the dominant 9-day singular vectors are only $O(100)$ (so that $T/(0.5 \log \sigma)$ is $O(3-5)$ days, where T is the integration time and σ is the singular value), dynamical models initialized with detailed information about the location of the Gulf Stream extension and its associated rings should produce useful forecasts over periods of $O(10-20)$ days. This is the approach taken by Robinson et al. (1989) in their work on forecast models for the Gulf Stream extension based on initialization with feature models. Our results suggest that such an approach could work well when one is interested in a regional forecast for a WBC extension or other strong open ocean front, and the region is either a significant distance downstream of any separation point or the separation point is locked by local topography. In a region such as the Malvinas Current – Brazil Current confluence of eastern South America, in which the latitudes of the separation points of the Brazil and Malvinas Currents are not strongly constrained by topography, information about larger scale structures, such as long barotropic Rossby waves in the adjacent ocean, are likely to be needed for accurate forecasting in the vicinity of the separation points.

Smoothed Time Series: 2-Layer QG Model

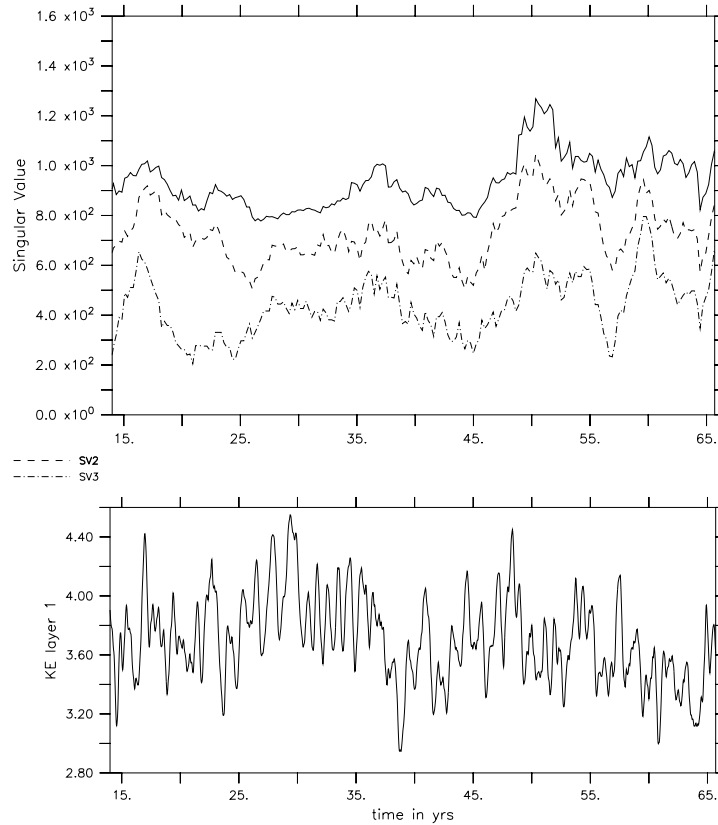


Fig. 13. Time series of the first three singular values (upper panel) and total kinetic energy of the 2LQG model in the strongly aperiodic regime ($\nu=10\text{ m}^2\text{ s}^{-1}$). The time series of the singular values smoothed using a running mean with a window of $t = 1100$ or 2.67 years to filter the high frequencies.

On a more abstract level, our results suggest that when one constructs assimilative forecast models of the behaviour of ocean fronts in a large domain, effectively reduced Kalman filters, which use a relatively small set of basis functions to represent both the data model misfit and the error covariance fields, are likely to be difficult to construct. The reason for this lies in the difficulty of representing strong local processes at time-varying locations with a small set of basis functions on a large domain. Well designed, ad hoc approaches, such as feature-based initialization or filters that use a larger number of static basis functions and a static error covariance matrix, while not as theoretically elegant as the full Kalman filter and its reduced space cousins, are likely to be more effective and more efficient.

References

- Arakawa, A.: Computational design for long-term integration of the equations of fluid motions, *Journal of Computational Physics*, 1, 119–143, 1966.
- Berloff, P. and Meacham, S.: On the stability of the wind-driven circulation, *Journal of Marine Research*, 56, 937–993, 1998.
- Charney, J.: The generation of oceanic currents by wind, *Journal of Marine Research*, 14, 477–498, 1955.
- Farrell, B.: Modal and non-modal baroclinic waves, *Journal of Atmospheric Science*, 41, 668–673, 1984.
- Farrell, B. and Ioannou, P.: Generalized stability theory. Part I: Autonomous operators, *Journal of Atmospheric Science*, 53, 2025–2040, 1996a.
- Farrell, B. and Ioannou, P.: Generalized stability theory. Part I: Nonautonomous operators, *Journal of Atmospheric Science*, 53, 2041–2053, 1996b.
- Farrell, B. and Moore, A.: An adjoint method for obtaining the most rapidly growing perturbation to oceanic flows, *Journal of Physical Oceanography*, 22, 338–349, 1992.
- Farrell, B. and Moore, A.: Rapid perturbation growth on spatially and temporally varying oceanic flows determined using an adjoint method: Application to the Gulf Stream, *Journal of Physical Oceanography*, 23, 1682–1702, 1993.
- Gustavsson, L.: Energy growth of 3-dimensional disturbances in plane poiseuille flow, *Journal of Fluid Mechanics*, 224, 241–260, 1991.
- Hansen, J. A. and Smith, L. A.: The role of operational constraints in selecting supplementary observations, *J. Atmos. Sci.*, 57, 2859–2871, 2000.
- Holland, W.: The role of mesoscale eddies in the general circulation of the ocean – Numerical experiments using a wind-driven quasigeostrophic model, *Journal of Physical Oceanography*, 8, 363–392, 1978.
- Ierley, G. and Young, W.: Viscous instabilities in the western boundary layer, *Journal of Physical Oceanography*, 21, 1323–1332, 1991.
- Lorenz, E.: A study of the predictability of a 28-variable atmospheric model, *Tellus*, 17, 321–333, 1965.
- Lorenz, E.: Barotropic instability of rossby wave motion, *Journal*

- of the Atmospheric Sciences, 29, 258–264, 1972.
- McCalpin, J. and Haidvogel, D.: Phenomenology of the low-frequency variability in a reduced gravity, quasigeostrophic double-gyre model, *Journal of Physical Oceanography*, 26, 739–752, 1996.
- Meacham, S.: Low-frequency variability in the wind-driven circulation, *Journal of Physical Oceanography*, 30, 269–293, 2000.
- Moore, A.: Wind-induced variability of ocean gyres, *Dynamics of Atmospheres and Oceans*, 29, 335–364, 1999.
- Moore, A. and Mariano, A.: The dynamics of error growth and predictability in a model of the Gulf Stream. part I: Singular vector analysis, *Journal of Physical Oceanography*, 29, 158–176, 1999.
- Orr, W.: The stability or instability of the steady motions of a perfect liquid and of a viscous liquid, *Proceedings of the Royal Irish Academy, A*, 27, 9–68, 1907.
- Palmer, T., Gelaro, R., Barkmeijer, J., and Buizza, R.: Singular vectors, metrics and adaptive observations, *Journal of the Atmospheric Sciences*, 55, 633–653, 1998.
- Pedlosky, J.: *Geophysical Fluid Dynamics*, Springer-Verlag, 1987.
- Primeau, F.: Multiple equilibria of a double-gyre ocean model with super-slip boundary conditions, *Journal of Physical Oceanography*, 28, 2130–2147, 1999.
- Robinson, A., Spall, M., and Pinardi, N.: Gulf stream simulations and the dynamics of ring and meander processes, *Journal of Physical Oceanography*, 18, 1811–1853, 1989.
- Trefethen, L., Trefethen, A., Reddy, S., and Driscoll, T.: Hydrodynamics stability without eigenvalues, *Science*, 261, 578–584, 1993.